Solid State Sciences 17 (2013) 67–71

Contents lists available at SciVerse ScienceDirect

Solid State Sciences

journal homepage: www.elsevier.com/locate/ssscie

Graphene anchored with $ZnFe_2O_4$ nanoparticles as a high-capacity anode material for lithium-ion batteries

Hui Xia [a,b,*], Yanyan Qian [a], Yongsheng Fu [b], Xin Wang [b,**]

[a] School of Materials Science and Engineering, Nanjing University of Science and Technology, 200 Xiaoling wei, Nanjing 210094, China
[b] Key Laboratory of Soft Chemistry and Functional Materials, Nanjing University of Science and Technology, Ministry of Education, Nanjing 210094, China

ARTICLE INFO

Article history:
Received 30 October 2012
Received in revised form
30 November 2012
Accepted 2 December 2012
Available online 12 December 2012

Keywords:
Zinc ferrite
Graphene
Anode material
Lithium-ion batteries
Nanocomposite

ABSTRACT

Heterostructured $ZnFe_2O_4$–graphene nanocomposites are synthesized by a facile hydrothermal method. The as-prepared $ZnFe_2O_4$–graphene nanocomposites are characterized by X-ray diffraction (XRD), transmission electron microscopy (TEM), Brunauer–Emmett–Teller (BET) analysis and galvanostatic charge and discharge measurements. Compared with the pure $ZnFe_2O_4$ nanoparticles, the $ZnFe_2O_4$–graphene nanocomposites exhibit much larger reversible capacity up to 980 mAh g^{-1}, greatly improved cycling stability, and excellent rate capability. The superior electrochemical performance of the $ZnFe_2O_4$–graphene nanocomposites could be attributed to the synergetic effect between the conducting graphene nanosheets and the $ZnFe_2O_4$ nanoparticles.

1. Introduction

Energy storage devices have attracted great attention due to the increasing demand for sustainable energy and renewable energy owing to the diminishing supply of fossil fuels and environmental degradation. Lithium-ion batteries (LIBs), one of the most promising energy storage devices, have been widely used as power sources for portable electronic devices such as mobile phones, laptops, digital cameras, and etc. [1,2]. The ever-growing need for high energy and/or high power for emerging new applications, such as electric vehicles, has prompted numerous research efforts toward developing new high performance electrode materials for the next generation LIBs. To date, graphite has been commonly used as anode material in the commercial LIBs, but the relatively low theoretical capacity of graphite (only about 372 mAh g^{-1}) has inspired intensive research efforts toward alternative anode materials [3–8]. Recently, zinc ferrite ($ZnFe_2O_4$) has attracted great attention due to its high theoretical capacity of about 1000 mAh g^{-1}, which is two times higher than that of graphite [9,10]. Like other high capacity transition metal oxides, $ZnFe_2O_4$ shows rapid capacity fading during cycling and reduced capacity at high charge/discharge rates due to the large volume change induced electrode pulverization and its poor electrical conductivity. Therefore, developing high performance $ZnFe_2O_4$ electrode material with both good cycling stability and rate capability remains a great challenge.

Graphene nanosheets, which possess a flexible porous texture, could be used as a confining structure with substantial buffering capability to reduce electrode pulverization [11]. Additionally, graphene nanosheets also have excellent electrical conductivity, large surface area, and chemical stability. Inspired by these virtues, graphene has been used as an excellent substrate to host active nanomaterials for energy storage applications [12]. It has been well demonstrated that the electrochemical performance of the metal oxide anodes for LIBs can be greatly improved by using the metal oxide–graphene nanocomposites [13,14]. However, to our best knowledge, the study of $ZnFe_2O_4$–graphene nanocomposites as anode material for LIBs has not been reported.

Herein, we report a one-step hydrothermal method for growing $ZnFe_2O_4$ nanoparticles on graphene nanosheets to form $ZnFe_2O_4$–graphene nanocomposites. Compared with the pure $ZnFe_2O_4$ nanoparticles, the $ZnFe_2O_4$–graphene nanocomposites exhibit a larger reversible capacity up to 980 mAh g^{-1}, greatly improved cycling stability, and excellent rate capability. The results indicate that the

* Corresponding author. School of Materials Science and Engineering, Nanjing University of Science and Technology, 200 Xiaoling wei, Nanjing 210094, China. Tel.: +86 25 84315606; fax: +86 25 84315159.
** Corresponding author. Tel.: +86 25 84305667; fax: +86 25 84315054.
E-mail addresses: xiahui@njust.edu.cn, jasonxiahui@gmail.com (H. Xia), wxin@public1.ptt.js.cn (X. Wang).

1293-2558/$ – see front matter © 2012 Elsevier Masson SAS. All rights reserved.
http://dx.doi.org/10.1016/j.solidstatesciences.2012.12.001

$ZnFe_2O_4$–graphene nanocomposite has great potential as anode material for the next generation high-performance lithium-ion batteries.

2. Experimental details

2.1. Synthesis of graphene oxide

Graphene oxide (GO) was synthesized from natural graphite powders by a modified Hummers method [15]. Briefly, 1.0 g graphite powder, 6.7 mL 98% H_2SO_4, 0.8 g $K_2S_2O_8$, and 0.8 g P_2O_5 were mixed to form a solution, which was maintained at 80 °C for 4.5 h. The resulting pre-oxidized product was cleaned with water and dried in a vacuum oven at 50 °C. After drying, 5.0 g $KMnO_4$, 40 mL 98% H_2SO_4, and 85 mL H_2O were mixed with the pre-oxidized product in sequence at a temperature below 20 °C. After 2 h of mixing, 150 mL H_2O and 8 mL 30% H_2O_2 were added into the mixture. After 10 min, a brilliant yellow solution was obtained. Then the resulting product was washed with diluted HCL aqueous solution and H_2O. The GO was obtained after drying the resultant in a vacuum oven at 30 °C for 10 h.

2.2. Synthesis of $ZnFe_2O_4$ nanoparticles and $ZnFe_2O_4$–graphene nanocomposites

The $ZnFe_2O_4$–graphene nanocomposites were synthesized by a straightforward hydrothermal method using ethanol–water as solvent. In a typical synthesis procedure, 80 mg GO was dispersed into 70 mL of absolute ethanol with sonication for 1 h. Then 0.8080 g $Fe(NO_3)_3 \cdot 9H_2O$ and 0.2975 g $Zn(NO_3)_2 \cdot 6H_2O$ were added into the GO dispersion solution with stirring for 30 min at room temperature, yielding a stable bottle-green homogeneous emulsion. The emulsion was transferred into a 100 mL Teflon-lined stainless steel autoclave and heated at 180 °C for 20 h under autogenous pressure. After cooling down to room temperature, the final product was filtered, washed with distilled water, and dried in a vacuum oven at 60 °C for 12 h $ZnFe_2O_4$ nanoparticles were prepared using a similar hydrothermal treatment without using GO.

2.3. Sample characterization

The microstructure and morphology of the products were characterized by X-ray diffraction (XRD), Raman spectroscopy and transmission electron microscopy (TEM). The powder XRD measurements were performed using a Bruker D8 advanced diffractometer with Cu Kα radiation with the scanning angle ranging from 5° to 80° of 2θ. The TEM investigations of different samples were carried out using a JEOL JEM2100 microscope. Raman spectra of different samples were acquired using a Renishaw invia Reflex Raman microprobe with a 532 nm wavelength incident laser. Nitrogen adsorption–desorption isotherms of different samples were measured using a Micromeritics Model TriStar II 3020 volumetric analyzer at 77 K.

2.4. Electrochemical measurements

Half cells using Li foil as both counter and reference electrodes were assembled with Lab-made Swagelok cells for electrochemical measurements. To make the working electrodes, 80 wt% active material ($ZnFe_2O_4$ nanoparticles and $ZnFe_2O_4$–graphene nanocomposite), 10 wt% acetylene black (Super-P), and 10 wt% polyvinylidene fluoride (PVDF) binder were mixed with N-methyl-2-pyrrolidinone (NMP). The obtained slurry was coated onto the Cu foils and dried at 120 °C for 2 h to remove the solvent. The electrodes were then pressed and cut into small disks (10 mm in diameter). The small disks were further dried at 80 °C in a vacuum oven for 12 h before battery tests. 1 M $LiPF_6$ in ethylene carbonate and diethyl carbonate (EC/DEC, v/v = 1:1) solution was used as the electrolyte and Celgard 2400 membrane was used as the separator. The cells were assembled in a glovebox where the moisture and oxygen concentrations were limited to below 1.0 ppm. The galvanostatic charge/discharge measurements were carried out on a LAND CT2001A electrochemical workstation with a voltage window between 0.01 and 3.0 V at different current densities at room temperature.

3. Results and discussion

Fig. 1 shows the XRD patterns of the GO, the reduced-GO, the pure $ZnFe_2O_4$ nanoparticles, and the $ZnFe_2O_4$–graphene nanocomposite. As shown in Fig. 1c, all diffraction peaks from the XRD pattern of the pure $ZnFe_2O_4$ nanoparticles can be indexed to a cubic structure of the $ZnFe_2O_4$ spinel (JCPDS No. 22-1010). Similar XRD pattern was obtained for the $ZnFe_2O_4$–graphene nanocomposite as shown in Fig. 1d. However, no typical diffraction peak of GO (001) (Fig. 1b) or grapene (002) (Fig. 1a) can be observed in the XRD pattern of the $ZnFe_2O_4$–graphene nanocomposite. The absence of GO (001) peak may be ascribed to the fact that GO was reduced to graphene during the hydrothermal reaction in the presence of alcohols [16,17]. On the other hand, during the hydrothermal reaction, crystal growth of $ZnFe_2O_4$ destroyed the regular layer stacking of reduced graphene oxide, leading to the exfoliation of graphene and the disappearance of the graphene (002) peak [18].

Fig. 2 shows the Raman spectra of the GO, the pure $ZnFe_2O_4$ nanoparticles, and the $ZnFe_2O_4$–graphene nanocomposite. The Raman spectra of the pure $ZnFe_2O_4$ nanoparticles (Fig. 2a) and the $ZnFe_2O_4$–graphene nanocomposite (Fig. 2c) show similar features in the frequency range of 100–1000 cm^{-1}, which are in good agreement with published works on $ZnFe_2O_4$ particles [19,20]. Wave numbers above 600 cm^{-1} are of the A1g mode, involving motions of the O in tetrahedral AO_4 groups. The other low-frequency phonon modes are due to metal ions involved in octahedral groups (BO_6), corresponding to the symmetric and antisymmetric bending of oxygen atoms in M-O bonds for octahedral groups [19,20].The Raman spectrum of the GO (Fig. 2b) shows two Raman bands at 1599 (G band) and 1362 cm^{-1} (D band), respectively, corresponding to the E_{2g} mode observed for sp^2 domains and the presence of sp^3 defects within the carbon. It has been reported that the G and D bands shift to lower frequency values when GO is reduced to graphene [21,22]. As shown in Fig. 2c, the D band shifts to 1347 cm^{-1} while the G band shifts to 1589 cm^{-1}, indicating that GO has been reduced to graphene in the $ZnFe_2O_4$–graphene nanocomposite. In addition, the

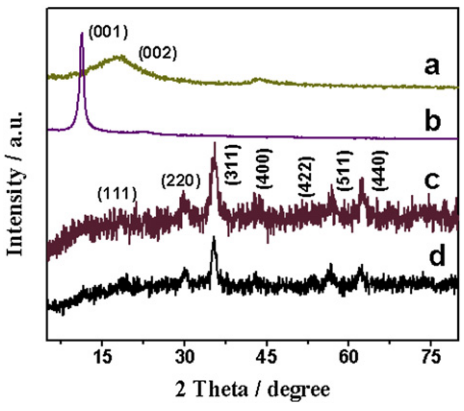

Fig. 1. XRD patterns of (a) the reduced GO, (b) the GO, (c) the pure $ZnFe_2O_4$ nanoparticles, and (d) the $ZnFe_2O_4$–graphene nanocomposite.

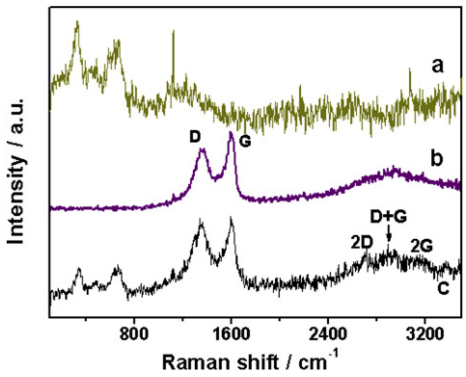

Fig. 2. Raman spectra of (a) the pure $ZnFe_2O_4$ nanoparticles, (b) the GO, and (c) the $ZnFe_2O_4$–graphene nanocomposite.

appearance of the 2D band at 2692 cm^{-1} in the Raman spectrum of the $ZnFe_2O_4$–graphene nanocomposite provides another evidence for the reduction of GO [23]. The peak position of 2D band is in good agreement with that of monolayer graphene [24,25]. The Raman results agree well with the XRD results, indicating the successfully synthesis of $ZnFe_2O_4$–graphene nanocomposite through the hydrothermal treatment.

The surface morphologies of the pure $ZnFe_2O_4$ nanoparticles and the $ZnFe_2O_4$–graphene nanocomposite were investigated by TEM. Fig. 3a and b show the TEM images of the pure $ZnFe_2O_4$ nanoparticles at low and high magnifications, respectively. It is clear to see that the $ZnFe_2O_4$ nanoparticles were produced after the hydrothermal treatment with severe aggregation. The typical particle size of the $ZnFe_2O_4$ nanoparticles is in the range of 20–30 nm in diameter. Fig. 3c and d show the TEM images of the $ZnFe_2O_4$–graphene nanocomposite at low and high magnifications, respectively. It is clear to see that the $ZnFe_2O_4$ nanoparticles are uniformly dispersed on the graphene nanosheets with much reduced aggregation. For the $ZnFe_2O_4$–graphene nanocompsoite, the almost transparent two-dimensional graphene nanosheets act as supporting substrates for homogeneously anchoring of $ZnFe_2O_4$ nanoparticles, building a $ZnFe_2O_4$–graphene heteroarchitecture. It is speculated that the introduction of graphene into $ZnFe_2O_4$ nanoparticles could improve the uniformity of $ZnFe_2O_4$ nanoparticles distribution on the graphene nanosheets and suppress the aggregation of $ZnFe_2O_4$ nanoparticles. It can be seen that the typical particle size of $ZnFe_2O_4$ nanoparticles in the nanocomposite is less than 10 nm, which is much smaller compared with that of the pure $ZnFe_2O_4$ nanoparticles. As shown in the inset in Fig. 3d, the HRTEM of a single $ZnFe_2O_4$ nanoparticle exhibits well-resolved lattice fringes with an interplane distance of 2.5 Å, which can be attributed to the (311) plane of the $ZnFe_2O_4$ crystal, indicating crystalline feature of the nanoparticles.

The specific surface areas of the pure GO, the pure $ZnFe_2O_4$ nanoparticles and the $ZnFe_2O_4$–graphene nanocomposite were obtained from the analysis of the desorption branch of N_2 gas isotherms using density function theory. As shown in Fig. 4, isotherms of both the pure $ZnFe_2O_4$ nanoparticles and the $ZnFe_2O_4$–graphene nanocomposite are typical for mesoporous materials with hysteresis loops at high partial pressures. According to Brunauer–Emmett–Teller (BET) analysis, a specific surface area of 181.7 $m^2\ g^{-1}$ is obtained for the $ZnFe_2O_4$–graphene nanocomposite, which is much larger than that of the pure $ZnFe_2O_4$ (74.5 $m^2\ g^{-1}$) nanoparticles. The small specific surface area of the pure $ZnFe_2O_4$ is probably due to the severe aggregation of nanoparticles. The BET specific surface area of the pure GO is only about 35.7 $m^2\ g^{-1}$, indicating that the GO sheets are not fully exfoliated. However, graphene itself has a large specific surface area as reported from literature [26]. When it is coupled with the $ZnFe_2O_4$, it can effectively reduce the aggregation of $ZnFe_2O_4$ nanoparticles as

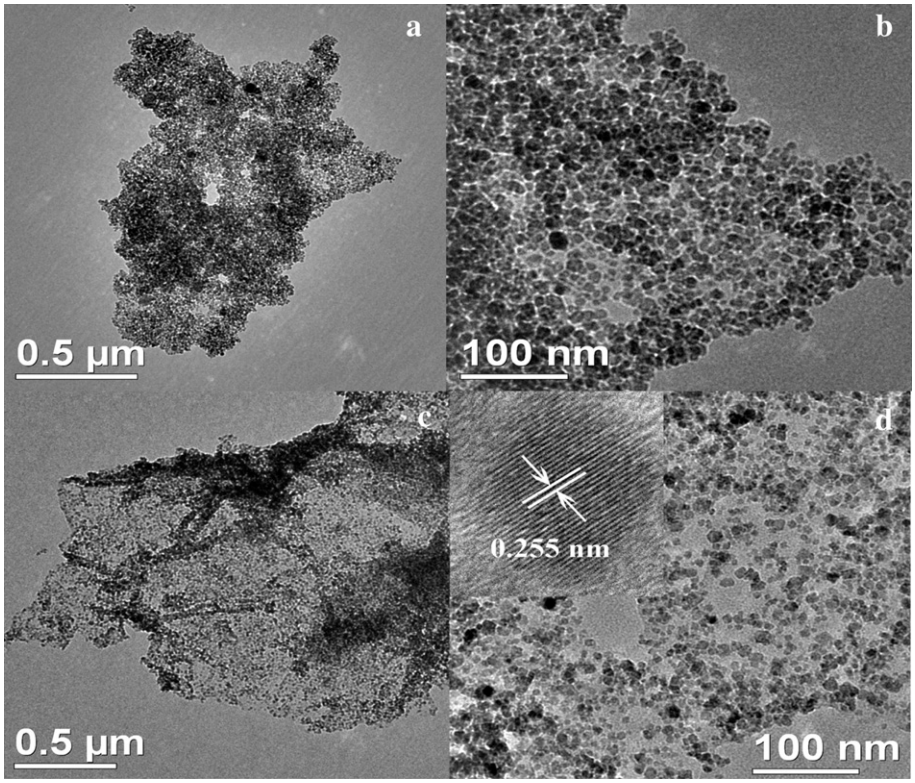

Fig. 3. TEM images of (a, b) the pure $ZnFe_2O_4$ nanoparticles and (c,d) the $ZnFe_2O_4$–graphene nanocomposite. (Inset in (d) is the TEM image of a single $ZnFe_2O_4$ nanoparticle attached on the graphene nanosheet).

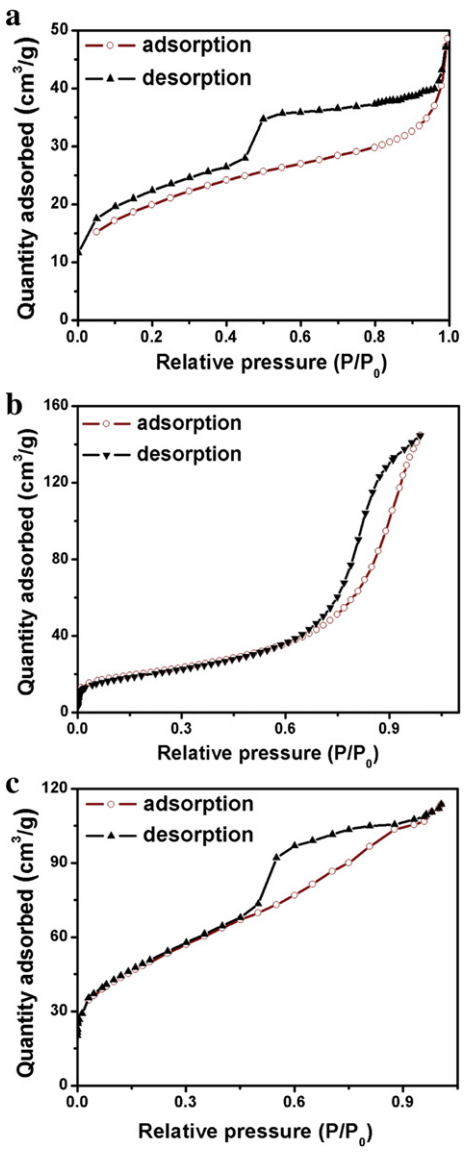

Fig. 4. Nitrogen adsorption–desorption isotherms of (a) the GO and(b) the pure $ZnFe_2O_4$ and (c) the $ZnFe_2O_4$–graphene nanocomposite.

observed from the TEM results, thus leading to a large specific surface area of the nanocomposite.

The $ZnFe_2O_4$–graphene nanocomposite could be a promising anode material for LIBs due to the synergetic effect between the highly conductive graphene nanosheets and $ZnFe_2O_4$ nanoparticles. In the present study, the electrochemical performance of the $ZnFe_2O_4$–graphene nanocomposite as anode material for LIBs was investigated. Fig. 5a and b show the charge/discharge curves of the pure $ZnFe_2O_4$ and $ZnFe_2O_4$–graphene nanocompsite electrodes, respectively, at the 1st, 2nd, 10th, 25th, and 50th cycles at a current density of 100 mA g^{-1} between 0.01 V and 3.00 V (vs. Li/Li^+). As shown in Fig. 5a, the first discharge and charge curves of the pure $ZnFe_2O_4$ electrode show voltage plateaus at about 0.8 and 1.7 V, respectively, corresponding to reduction/oxidation reactions during lithium insertion/extraction [27,28]. The first discharge and charge capacities of the pure $ZnFe_2O_4$ electrode are 1259 and 745 mAh g^{-1}, respectively, with a coulombic efficiency of 59.2%. The irreversible capacity loss for the first cycle is probably due to incomplete conversion reaction and the solid electrolyte interface (SEI) layer formation at the electrode/electrolyte interface caused by the reduction of electrolyte [29]. As shown in Fig. 5b, the charge/discharge curves of the $ZnFe_2O_4$–graphene nanocomposite electrode show similar voltage plateaus as the pure $ZnFe_2O_4$ electrode, indicating similar redox reactions occur during the charge/discharge processes. The first discharge and charge capacities of the $ZnFe_2O_4$–graphene nanocomposite electrode are 1376 and 945 mAh g^{-1}, respectively, with a coulombic efficiency of 68.6%. Fig. 5c compares the cycle performance between the pure $ZnFe_2O_4$ electrode and the $ZnFe_2O_4$–graphene nanocomposite electrode. After 50 cycles, the pure $ZnFe_2O_4$ electrode can only deliver a reversible capacity of about 237 mAh g^{-1}, which is only 16.8% of the reversible capacity for the first cycle. For the $ZnFe_2O_4$–graphene nanocomposite electrode, the reversible capacity increases initially and reaches a maximum of about 1078 mAh g^{-1} then decreases slowly with further cycling. This phenomenon that the reversible capacity of transition metal oxide electrode increases with cycling was also observed by Zhou et al. [30]. This is referred as an electrode activation process. As discussed by Do and Weng [31], when sufficient graphene nanosheets (20 wt %) is supplied in the electrode, the configuration of the metal oxide electrode could rearrange, which results in increased contact between active material and electrolyte with cycling. In the present study, the $ZnFe_2O_4$–graphene could also go through the activation process during the initial charge/discharge cycles with capacity increase. After 50 cycles, the reversible capacity of the $ZnFe_2O_4$–graphene nanocomposite electrode is about 956 mAh g^{-1}, which is still higher than that of the first cycle. As shown in Fig. 5d, the $ZnFe_2O_4$–graphene nanocomposite electrode also exhibits greatly enhanced rate capability compared with the pure $ZnFe_2O_4$ electrode. Even at a high current density of 1000 mA g^{-1}, the $ZnFe_2O_4$–graphene electrode can still deliver a reversible capacity of about 600 mAh g^{-1}, which is much higher than that of the pure $ZnFe_2O_4$ electrode (185 mAh g^{-1}).

The superior electrochemical performance of the $ZnFe_2O_4$–graphene nanocomposite as anode for LIBs can be attributed to the synergetic effect between the conducting graphene nanosheets and the $ZnFe_2O_4$ nanoparticles. $ZnFe_2O_4$ nanoparticles could provide a large electrode/electrolyte interface area and shortened lithium ion diffusion paths. However, the aggregation of $ZnFe_2O_4$ nanoparticles is clearly observed in the pure $ZnFe_2O_4$. The aggregation of nanoparticles induces big clusters of several hundred nanometers in size, which could block the penetration of electrolyte, leading to a reduced electrode/electrolyte interface area. In addition, the formed clusters could be pulverized due to large volume change induced by the charge/discharge processes, which could lead to the loss of electrical contact between $ZnFe_2O_4$ nanoparticles and current collector, thus resulting in fast capacity fading as observed in Fig. 5c. In the nanocomposite, however, the graphene nanosheets can effectively suppress the aggregation of $ZnFe_2O_4$ nanoparticles. The $ZnFe_2O_4$–graphene heteroarchitecture not only suppresses the aggregation of $ZnFe_2O_4$ nanoparticles but also prevents the restacking of graphene nanosheets, resulting in a large electrode/electrolyte interface area. The large interface area not only provides more Li^+ insertion/extraction sites, but also facilitates fast Li^+ ion transfer between electrode and electrolyte, thus leading to a large reversible capacity of the nanocomposite electrode [32]. The two-dimensional graphene nanosheets in the $ZnFe_2O_4$–graphene nanocomposite with excellent electrical conductivity can serve as the conductive medium between the $ZnFe_2O_4$ nanoparticles and the current collector. The charge carriers could be effectively and rapidly conducted back and forth from the $ZnFe_2O_4$ nanoparticles to the current collector through the highly conductive graphene nanosheets, resulting in good rate capability [33]. With numerous voids between $ZnFe_2O_4$ nanopartilces and graphene nanosheets working as an elastic buffer, the $ZnFe_2O_4$–graphene nanocomposite electrode could accommodate larger volume expansion/contraction compared with the pure $ZnFe_2O_4$ electrode, thus leading to excellent cycling stability.

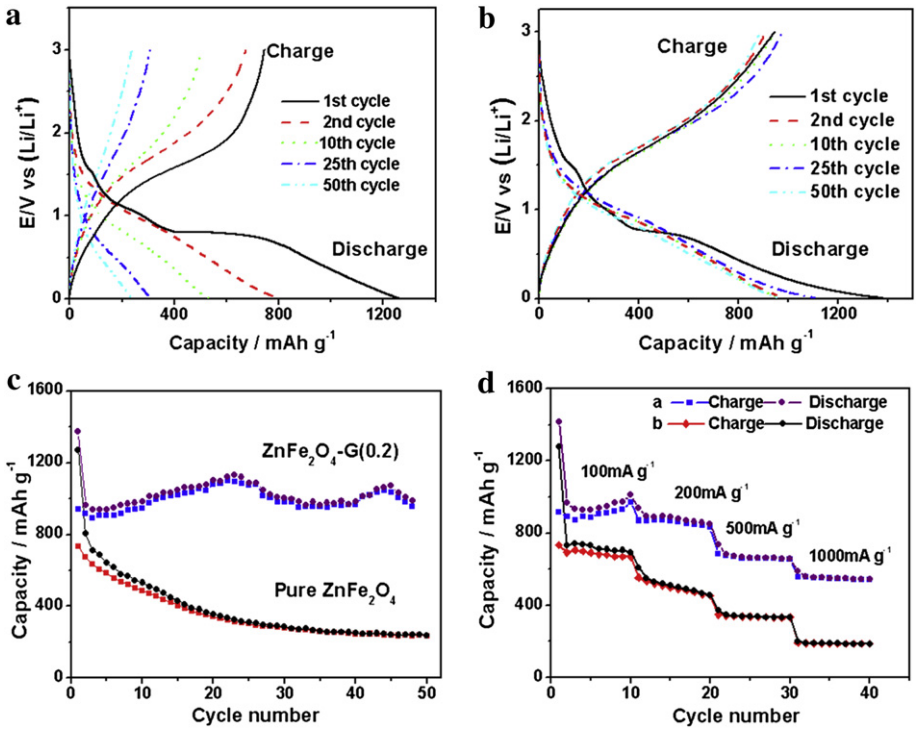

Fig. 5. Charge/discharge curves of (a) the pure $ZnFe_2O_4$ electrode and (b) the $ZnFe_2O_4$–graphene nanocomposite electrode. (c) Cycle performance of the pure $ZnFe_2O_4$ electrode and the $ZnFe_2O_4$–graphene nanocomposite electrode. (d) Rate capability of the pure $ZnFe_2O_4$ electrode and the $ZnFe_2O_4$–graphene nanocomposite electrode.

4. Conclusions

$ZnFe_2O_4$–graphene nanocomposites with $ZnFe_2O_4$ nanoparticles anchored on the graphene nanosheets have been successfully synthesized by a simple hydrothermal strategy. It was found that the graphene plays an important role in suppressing the aggregation of $ZnFe_2O_4$ nanoparticles. The $ZnFe_2O_4$–graphene nanocomposite electrode exhibited a high reversible capacity up to 1082 mAh g^{-1} with good rate capability and excellent cycling stability. The superior anode performance of the $ZnFe_2O_4$–graphene nanocomposite is due to the synergetic effect between the conducting graphene nanosheets and $ZnFe_2O_4$ nanoparticles, which makes the $ZnFe_2O_4$–graphene nanocomposite a promising anode material for the next-generation lithium-ion batteries.

Acknowledgments

This investigation was supported by the National Natural Science Foundation of China (No. 21171094, 51102134), A Project Funded by the Priority Academic Program Development of Jiangsu Higher Education Institutions, NUST Research Funding (2011PYXM03, 2011ZDJH21) and the Department of Education of Jiangsu Province (CXZZ11_0245).

References

[1] C. Liu, F. Li, L.P. Ma, H.M. Chen, Adv. Mater. 22 (2010) 28.
[2] F.Y. Cheng, J. Liang, Z.L. Tao, J. Chen, Adv. Mater. 23 (2011) 1695.
[3] P.N. Zhu, Y.Z. Wu, M.V. Reddy, A.S. Nair, B.V.R. Chowdari, S. Ramakrishna, RSC Adv. 2 (2012) 531.
[4] J.K. Feng, M.O. Lai, L. Lu, Electrochim. Acta 62 (2012) 103.
[5] Y. Wang, H.J. Zhang, L. Lu, L.P. Stubbs, C.C. Wong, J.Y. Lin, ACS Nano 4 (2010) 4753.
[6] J.P. Liu, J. Jiang, C.W. Cheng, H.X. Li, J.X. Zhang, H. Gong, H.J. Fan, Adv. Mater. 23 (2011) 2076.
[7] L. Zhou, D.Y. Zhao, X.W. Lou, Adv. Mater. 24 (2012) 745.
[8] B.K. Guo, X.P. Fang, B. Li, Y.F. Shi, C.Y. Ouyang, Y.S. Hu, Z.X. Wang, G.D. Stucky, L.Q. Chen, Chem. Mater. 24 (2012) 457.
[9] Y. Sharma, N. Sharma, G.V.S. Rao, B.V.R. Chowdari, Electrochim. Acta 53 (2008) 2380.
[10] Y.F. Deng, Q.M. Zhang, S.D. Tang, L.T. Zhang, S.N. Deng, Z.C. Shi, G.H. Cheng, Chem. Commun. 47 (2011) 6828.
[11] L.L. Tian, Q.C. Zhuang, J. Li, C. Wu, Y.L. Shi, S.G. Sun, Electrochim. Acta 65 (2012) 153.
[12] Z.S. Wu, W.C. Ren, L. Wen, L.B. Gao, J.P. Zhao, Z.P. Chen, G.M. Zhou, F. Li, H.M. Cheng, ACS Nano 4 (2010) 3187.
[13] Y. Xu, R. Yi, B. Yuan, X.F. Wu, M. Dunwell, Q.L. Lin, L. Fei, S.G. Deng, P. Andersen, D.H. Wang, H.M. Luo, J. Phys. Chem. Lett. 3 (2012) 309.
[14] L. Li, Z.P. Guo, A.J. Du, H.K. Liu, J. Mater. Chem. 22 (2012) 3600.
[15] W.S. Hummers, R.E. Oeman, J. Am. Chem. Soc. 80 (1958) 1339.
[16] H. Zhang, X. Lv, Y. Li, Y. Wang, J. Li, ACS Nano 4 (2010) 380.
[17] Y. Zhang, Z.R. Tang, X. Fu, Y.J. Xu, ACS Nano 4 (2010) 7303.
[18] Y.S. Fu, X. Wang, Ind. Eng. Chem. Res. 50 (2011) 7210.
[19] Z.W. Wang, D. Schiferl, Y.S. Zhao, H.S.C. O'Neill, J. Phys. Chem. Solids 64 (2003) 2517.
[20] M. Maletin, E.G. Moshopoulou, A.G. Kontos, E. Devlin, A. Delimitis, V.T. Zaspalis, L. Nalbandian, V.V. Srdic, J. Eur. Ceram. Soc. 27 (2007) 4391.
[21] S. Stankovich, D.A. Dikin, R.D. Piner, K.A. Kohlhaas, A. Kleinhammes, Y. Jia, Y. Wu, S.T. Nguyen, R.S. Ruo, Carbon 45 (2007) 1558.
[22] T.N. Lambert, C.A. Chavez, B. Hernandez-Sanchez, P. Lu, N.S. Bell, A. Ambrosini, T. Friedman, T.J. Boyle, D.R. Wheeler, D.L. Huber, J. Phys. Chem. C 113 (2009) 19812.
[23] Y.S. Fu, H.Q. Chen, X.Q. Sun, X. Wang, Appl. Catal. B 111-112 (2012) 280.
[24] K.S. Vasu, B. Chakraborty, S. Sampath, A.K. Sood, Solid State Commun. 150 (2010) 1295.
[25] A.C. Ferrari, J.C. Meyer, V. Scardaci, C. Casiraghi, M. Lazzeri, F. Mauri, S. Piscanec, D. Jiang, K.S. Novoselov, S. Roth, A.K. Geim, Phys. Rev. Lett. 97 (2006) 187401.
[26] P.C. Lian, X.F. Zhu, S.Z. Liang, Z. Li, W.S. Yang, H.H. Wang, Electrochim. Acta 55 (2010) 3909.
[27] X.W. Guo, X. Lu, X.P. Fang, Y. Mao, Z.X. Wang, L.Q. Chen, X.X. Xu, H. Yang, Y.N. Liu, Electrochem. Commun. 12 (2010) 847.
[28] Y. Ding, Y.F. Yang, H.X. Shao, Electrochim. Acta 56 (2011) 9433.
[29] Y.G. Guo, J.S. Hu, L. Wan, Adv. Mater. 20 (2008) 2878.
[30] G.M. Zhou, D.W. Wang, F. Li, L.L. Zhang, N. Li, Z.S. Wu, L. Wen, G.Q. Lu, H.M. Cheng, Chem. Mater. 18 (2010) 5306.
[31] J.S. Do, C.H. Weng, J. Power Sources 146 (2005) 482.
[32] X.J. Zhu, Y.W. Zhu, S. Murali, Meryl D. Stoller, Rodney S. Ruoff, ACS Nano 4 (2011) 3333.
[33] H.L. Wang, L.F. Cui, Y. Yang, H.S. Casalongue, J.T. Robinson, Y.Y. Liang, Y. Cui, H.J. Dai, J. Am. Chem. Soc. 132 (2010) 13978.